Input characterisation for low-amplitude seismicity induced by geothermal operations

F. Taddei [1], **A. Kumawat** [1], **A. Csuka** [2], **R. Cudmani** [2], **G. Müller** [1]
[1] Technical University of Munich, Chair of Structural Mechanics,
Arcisstrasse 21, 80333, Munich, Germany
e-mail: **francesca.taddei@tum.de**

[2] Technical University of Munich, Chair of Soil Mechanics and Foundation Engineering,
Rock Mechanics and Tunneling,
Franz-Langinger-Str. 10, 81245, Munich, Germany

Abstract
The risk assessment of buildings subjected to low-amplitude geothermal-induced (GI) seismic events relays on the knowledge of fragility functions for serviceability and comfort, exposure models and input ground motions. The latter must be specifically estimated for induced seismicity in geothermal reservoirs and differ substantially from those related to tectonic events. The modelling of the input ground motions has an influence on the idealization of the buildings and the soil-structure interaction used for the risk assessment. This contribution addresses open questions about the spectral characteristics and the predominant polarization of the low-amplitude short-duration signals, considering an exemplary seismic data set from the Insheim geothermal reservoirs in Germany. It gives the seismological characteristics, the statistical evaluation of the spectral content and the elastic response spectra for the selected events and sites, and the resulting practical suggestions for the modelling of the input for building risk assessment in case of GI seismicity.

1 Introduction

Deep geothermal energy represents a sustainable energy supply and an alternative to fossil fuels, especially for heating purposes. It is not affected by seasonal changes or weather conditions and exploitation activities do not deplete it [1]. Its extraction involves boreholes with depths of more than 400 m. The borehole drilling and the operation of a Geothermal Power Plant (GPP) can cause ruptures in the underground. In the injection of could fluid in the well, the rock mass is subjected to injection pressures and thermal stress, which, in turn, cause cracks processes. These induce microseismic activity in the nearby underground area [2]. In general, the dominant value of moment magnitude for Geothermal-Induced (GI) events varies from 1 to 3; however, it is not unexpected for GPPs induced earthquakes to have a more significant magnitude. In addition, the focal depth of GPP earthquakes usually ranges from 1 to 10 km, depending on the local geophysical conditions and the injection wells depth. Moreover, the epicenters of earthquakes are very close to the GPPs stations, mostly less than 10 km [3].

For the optimal distribution of energy for heating, GPPs are usually located close to urban areas and, therefore, the microseismic activity can be felt by the communities even at low magnitudes [4]. It is important to investigate the many uncertainty of this process and address the public concern about the occurrence of perceptible induced seismicity at GPP sites. In Germany, several GPPs in Basel, Landau, Insheim and Unteraching have been in the spotlight of the community worry in the last decade. However, it must be pointed out, that, when compared to all other types of seismicity, its risk is very low. In a large study on induced seismicity in Central Europe, it was shown that, the maximum observed magnitude of induced seismicity at geothermal sites is the smallest of the possible types of induced/triggered seismicity and significantly smaller than the values for natural tectonic earthquakes for the investigated sites [4]. For GI events in Central Europe,

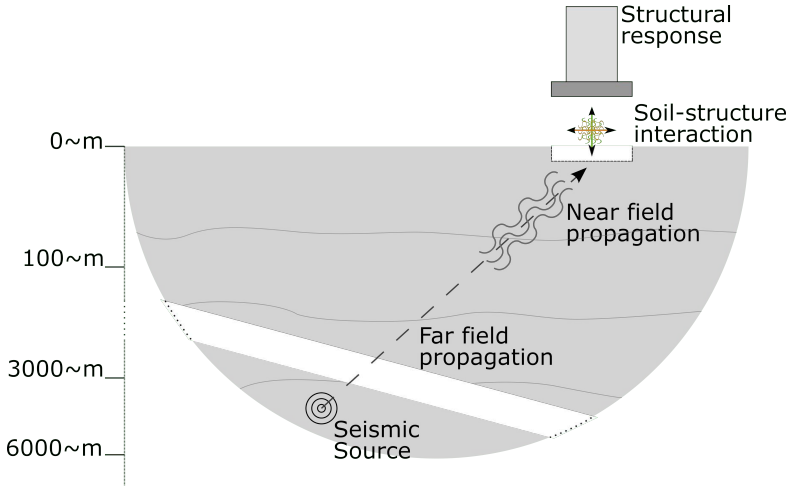

Figure 1: Depiction of the problem.

the observed or predicted microseismic intensities are usually well below the range where structural damage can occur [4]. However, comfort problems for the community can represent a limit for the operation of the GPP, causing economic losses [3].

This contribution addresses one specific aspect related to GI seismicity, which is the characterisation of the input ground motion for risk assessment of buildings subjected to low-amplitude GI seismic events.

It is recognized, that, for tectonic events, the frequency content, the duration and the direction of the seismic action can play an important role for the building response [5]. However, for GI events, very limited knowledge exists about the seismic building response, due to the very low impact of the microseismic activity. Seismic hazard assessment models and ground motion models for GI have been proposed in recent studies [6, 7]. However, site-specific investigations are necessary for a more accurate assessment of the building vibrations. The risk analysis for building subjected to induced seismicity requires an iterative modelling process, as the detail degree of the building model depends on the type of excitation and, vice-versa, the level of details for the modelling of the excitation depends on the sought analysis outcome. Moreover, the wave propagation process from the seismic source to the building foundation can have a large influence on the vibrational input at the foundation level. Fig. 1 depicts the general problem.

The main objective of this research work is to extend the knowledge about the input ground motion for GI, by answering the following two questions:

1. Which spectral characteristics are exhibited by the low-amplitude signals related to the GI seismicity? How do they influence the choice of the modelling of the building-foundation system?

2. Is there a predominant polarization of the seismic waves that could suggest a one-dimensional problem? Or is a three-dimensional behavior the only realistic scenario?

Using recorded data for the Insheim geothermal reservoir in Germany, this investigations shows the most important seismological characteristics, the statistical evaluation of the spectral content as a function of magnitude and site-to-source distance and the elastic response spectra for the selected GI events and stations.

2 Induced seismicity at the Insheim geothermal reservoir

The Upper Rhine Graben (URG) represent the most exploited area for geothermal energy production in Germany, thanks to high geothermal gradient, where more than 150° are reached at depths of 2500 m in the northern part of the URG. Tab. 1 gives the key data of the Insheim geothermal power plan. Even if the URG

Table 1: Key data of the Insheim geothermal power plan.

Geothermal area	Country	Start date	Lat (°)	Lon (°)	Max. well depth (m)
Upper Rhine Graben	DE	2007	49.15	8.15	3800

is one of the most seismically active regions in Germany, the seismic risk is small to moderate compared to the tectonic European scale. Since the begin of the activity of the Insheim and Landau geothermal reservoirs in the URG in 2006, more than 2200 induced microevents have been detected in the vicinity of the reservoirs. Among these, several events with a magnitude larger than 2 have been recorded in Insheim. [8]

2.1 Seismic networks in the vicinity of the Insheim GPP

The majority of these events has a local magnitudes M less than 1.0 and the largest event in Insheim had a magnitude of ML$\approx$ 2.4. Most of the events occurred along a fault zone between the injection and the production wells and are aligned NNW-SSE [9]. The low signal-to-noise ratio causes difficulties for the application of classical methods for tectonic earthquakes, for example for the localisation [10].

2.2 Seismic monitoring

Only few microevents in Insheim were perceived by the local population, but the public concern for the large number of microevents led to a reduction of the production rate of the power plant and a long-term seismic monitoring [8]. Near the GPP, there are several seismological networks and borehole stations from public agencies and a private special immission data network for the recording of ground vibration velocities according to the German DIN4150 standards [11]. To account for the high frequency content and short duration of small events, the sampling rate is set to 200 Hz at most stations [8]. Tab. 2 gives the list of selected past and current installed networks and corresponding stations.

Table 2: List of stations in the vicinity of the Insheim GPP and corresponding data information.

Operator	Stations	Network	Availability	Channel inventory
BGR[2]	INS1, INS2, INS3, INS4, INS4B, INS5, INS6, INS6B, INS7, INS8, INS9, INSH, LDAU, TMO20, TMO22, TMO54, TMO55, TMO57, TMO66	GR[12]	Public (ORFEUS)	Public (EIDA)[13]
LER	IMS, FACH, FSH, RIVT , ROTT, LDE	-	Public (contact)	Public (contact)
Private stations	ST1, NOS2, SOS2 and Immission network	-	Private	Private
ETH Zurich	A127A	Z3	Public (ORFEUS)	Public (EIDA)[13]

3 Ground motion samples for the Insheim area

This study considers only public data available from selected stations, which are shown in Fig. 2 along with the location of the considered GPP. The data are retrieved from the ORFEUS database [14]. The following steps led to the data retrieval:

1. create a catalogue of events of interest using, for example, the database of the local earthquakes of the State Authority for Geology and Mining Rhineland-Palatinate (LGBRLP). Here, one can find all

local events in Rhineland-Palatinate, Baden-Württemberg and within a distance of up to 1000 km from these regions.

2. supply the event catalogue into the European Integrated Data Archive (EIDA) through the web interface, which is integrated in ORFEUS [15].

3. select the stations of interest in the EIDA web interface. Here, all the stations in the region with latitude between 49°00' and 49°20' and longitude between 7°50' and 8°20' were selected.

4. request wave forms relative to the supplied event start time and selected station and download raw data in .mseed format.

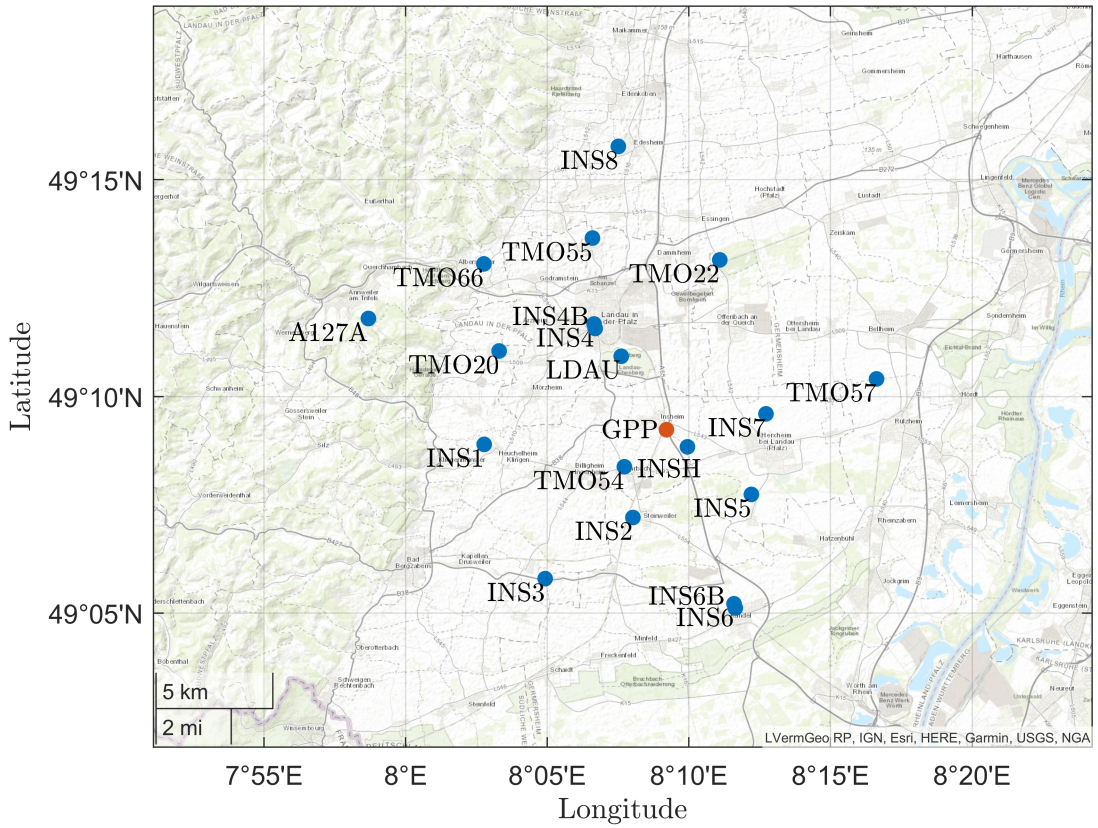

Figure 2: Map of the selected stations for this study (blue dots) and location of the Insheim GPP (red dot). See also Tab. 2.

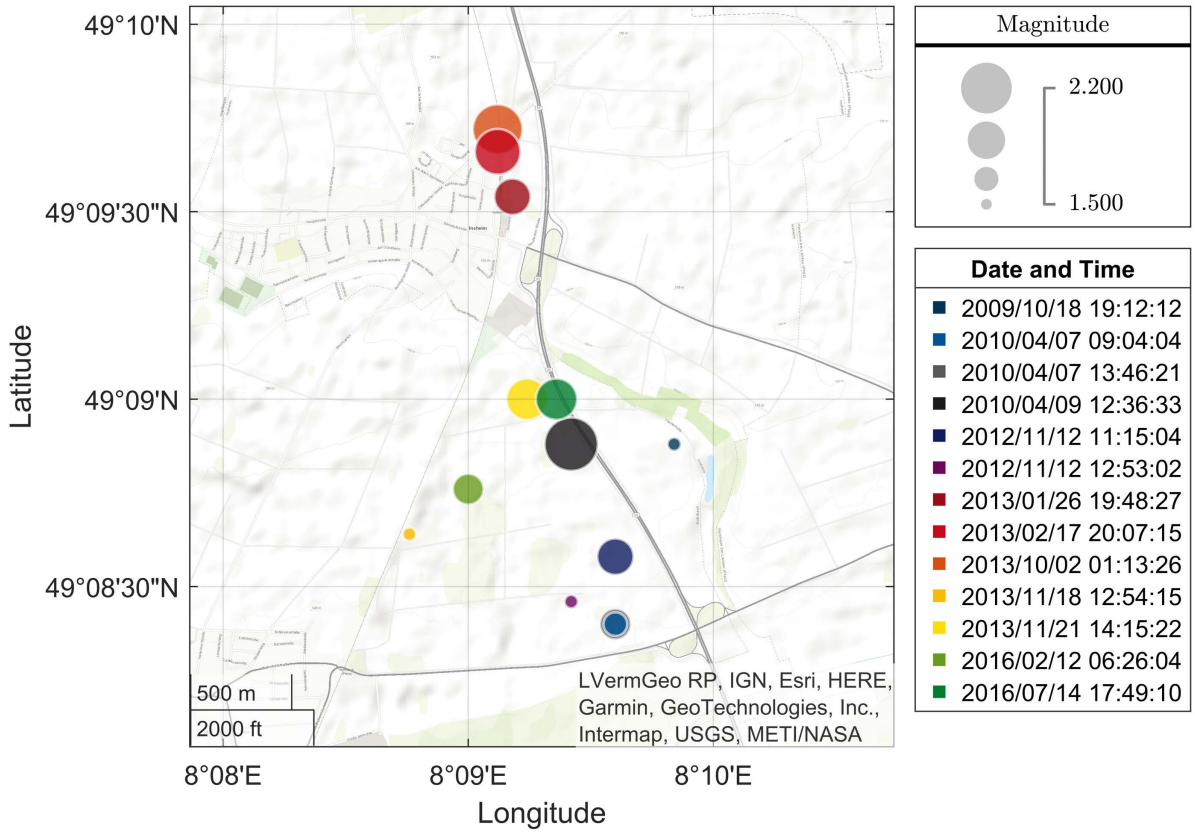

Figure 3: Geographical distribution of the selected events with the corresponding local magnitude M and start time.

The 17 selected events have local magnitude values M from a minimum of 1.5 to a maximum of 2.4 and occurred within a radius of 2 km from the Insheim GPP (lat.$=49.15°$, lon.$=8.15°$, see also Tab. 1 and Fig. 2). After requesting the wave forms for the 17 selected events in ORFEUS, recordings of at least one station were available only for 13 events. The events catalogue is shown in Tab. 3 in the annex and a number is assigned only to the events with available recordings. The time is always given in terms of local time. Fig. 3 shows the geographical distribution of the selected events with the corresponding local magnitude M and start time.

The quality and reliability of the raw data was verified and improved with a wavelet denoising, baseline adjustment and a high-pass filtering, as described in [16, 7]. This procedure was successfully implemented in the past for both low-amplitude GI seismic recordings and low-intensity signals of the Iranian plateau. In some cases, the stations are equipped with several sensors with different properties. These are identified with channel codes after [17]. In the further discussion, for each event and for each station, we consider only one recording in each direction (Z for vertical, N for north-south and E for east-west) with sample rate between 80 and 250 Hz and corner period < 10 s. Tab. 4 in the annex shows the list of recording stations for each event.

After reviewing the processed available data, the ground motions for the event n. 4 with start time 2010/04/09, 12:36:33, recorded at the single station LDAU, showed incongruous transient behaviour and were discarded. Therefore, the maximum magnitude considered in this study is 2.1. The usable data constitute a database of 12 events and 94 sets of 3 recordings in Z, N and E directions. Fig. 4 shows an example of vertical seismograms for the event n.9 with start time 2013/10/02, 12:36:33. One can observe the short duration of the earthquake and the fast decrement of the amplitudes of the signals as the distance from the epicenter increases. In the following section, aspects of the statistical evaluation of the database are discussed.

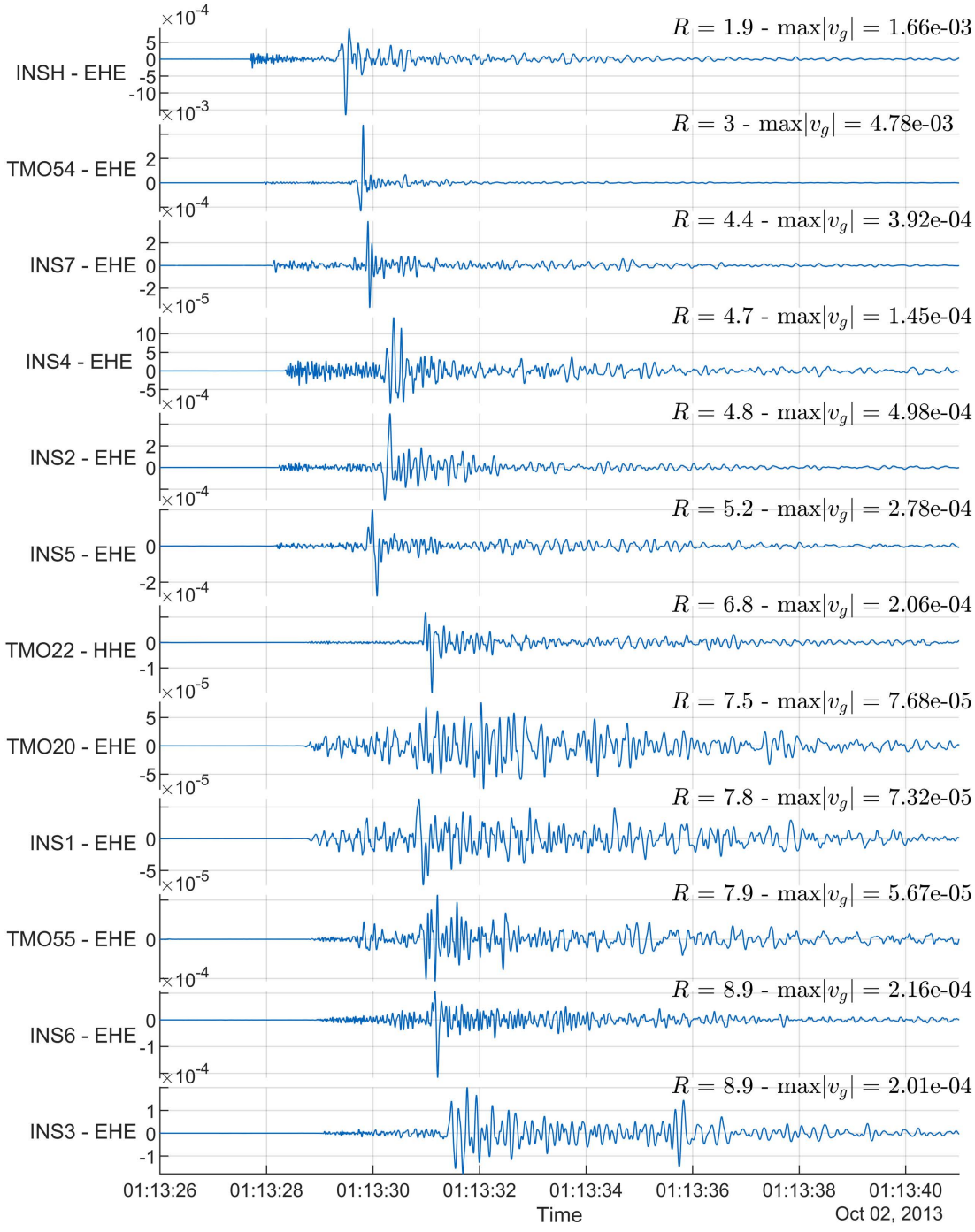

Figure 4: Exemplary ground velocities $v_g(t)$ in m/s, in Z-direction, for the event n. 9 with start time 2013/10/02, 12:36:33. R gives the site-to-source distance in km. The maximum of the absolute of each signal, $\max|v_g|$ is given in m/s. The signals are sorted from the closest stations to the epicenter at the top to the furthest at the bottom.

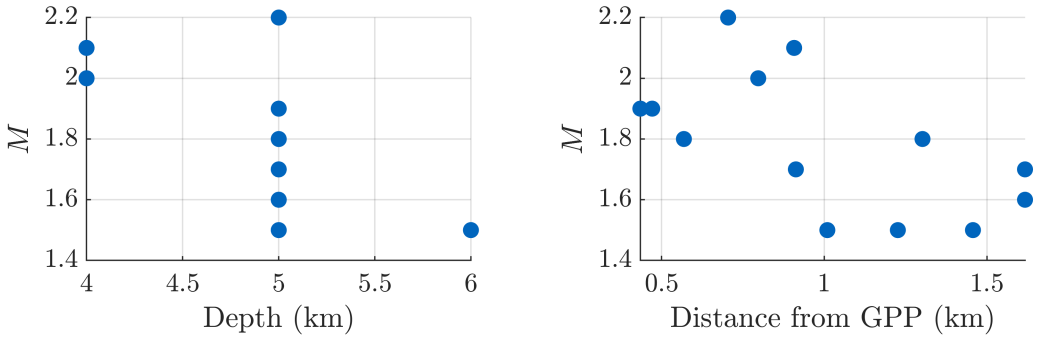

Figure 5: Distribution of the magnitude of the selected events w.r.t. a) the event depth in km and b) the distance form the GPP in km.

4 Ground motions elaboration

4.1 Events and ground motions characteristics

The events are characterized through the local magnitude M, the depth and the distance from the GPP. Fig. 5 shows that the majority of the events occur at 5 km depth and that the events with the highest magnitude are the closest to the GPP. The distance from the GPP falls into a narrow interval between 0.5 and 1.5 km.

The ground motions are characterized through the site-to-source distance R in km, the Peak Ground Velocity (PGV) in m/s and the Peak Ground Acceleration (PGA) in m/s^2, the Arias Intensity I_a in m/s and the duration D in s. Fig. 6 shows the distribution of these parameters w.r.t the R parameter, for all the directions of motion. The color of the dots represents the magnitude M. As expected, for larger distances from the sources, the signals exhibit on average smaller PGV and PGA. The blue dots draw the lower bound, while the green dots represent the upper bound of the descending curves. All the signals have a duration smaller than 10 s, which, on average, is shorter than the duration of tectonic events. There is a slight tendency of an increasing duration with increasing site-to-source distance R. Fig. 7 shows the distribution of the same parameters w.r.t. the M parameter. The color of the dots represents the value of R. Referring to the German standard DIN 4150-3 [11], in order to exclude possible damage to normal residential buildings, the ground velocities at the foundation should not exceed the value of 5 mm/s [18]. This value was exceeded only for the single case of $M = 2.1$ and $R = 2.5$, as shown in the plots.

4.2 Spectral content of the ground motions

The spectra of the recordings help to identify the frequency range of interest and possible amplification effects. The resultant in the horizontal direction is computed as the geometric mean of the spectral ordinates of the two as-recorded horizontal components E and N. This is acceptable as long as the ground motion directionality is small, which is assumed in this study. Fig. 8 shows the spectra of the horizontal resultants of the recordings sorted according to 3 categories for the distance R ($R \leq$3 km, 3 km$< R <$5 km,$R \geq$5 km). For each category, the spectra of the single events and the average are shown. Fig. 8a and Fig. 8b show the recordings of the event with $M \geq 1.9$ and $M < 1.9$ respectively. The same is shown for the vertical components in Fig. 9. In general, the maxima of the spectra are concentrated in the range between 1 and 40 Hz, as also found in [18]. The maxima of the horizontal spectra are rather concentrated in a narrow frequency range below 15 Hz, while the vertical spectra are spread over a broad frequency band up to 30 Hz. As many natural bending modes of ceiling for residential buildings have frequencies between 10 and 40 Hz, the broad band vertical spectra indicate a possible activation of those modes and the vertical vibrations of the ceiling could constitute a relevant contribution to the overall building response.

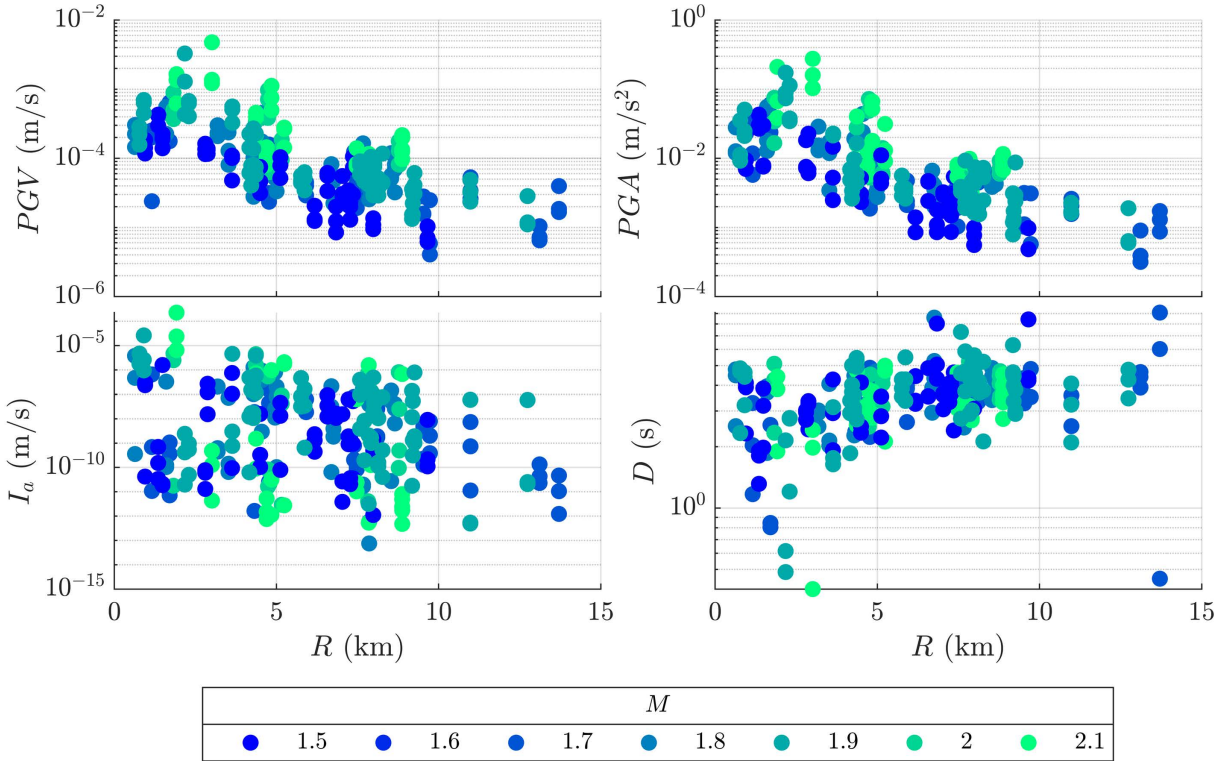

Figure 6: Distribution of PGV, PGA, I_a and D as a function of the site-to-source distance R and for different magnitudes M, indicated with different colors.

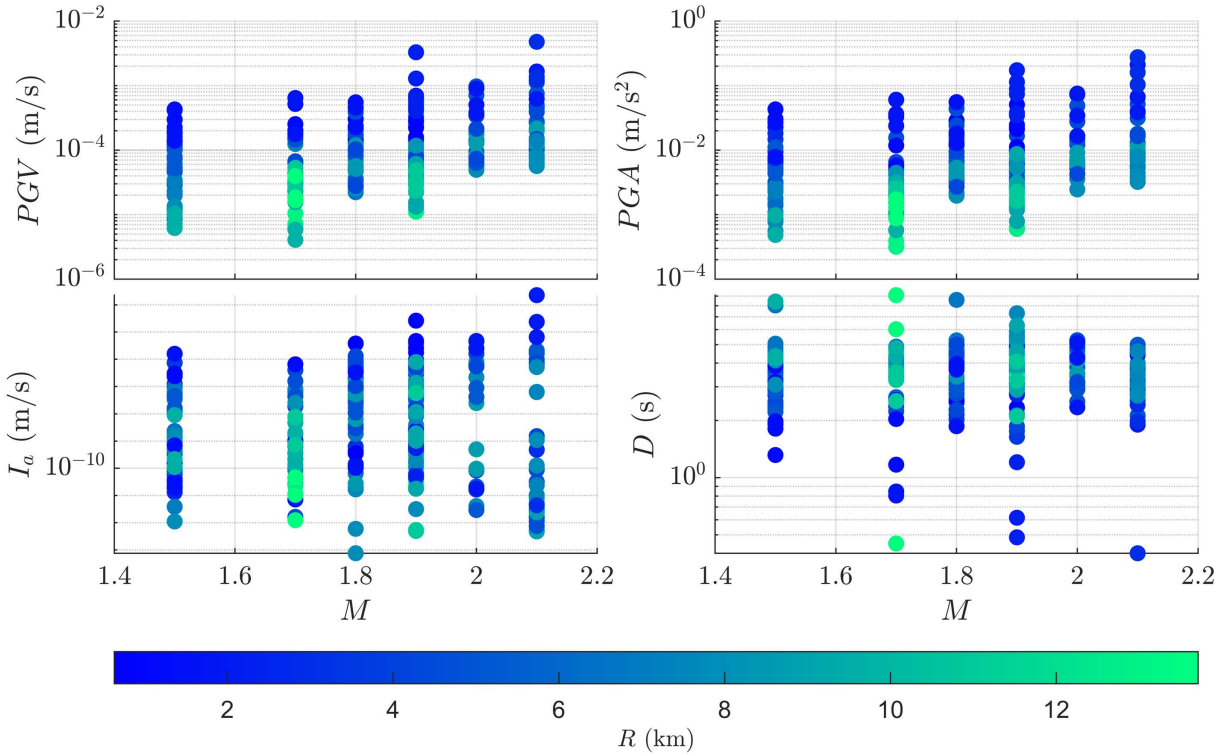

Figure 7: Distribution of PGV, PGA, I_a and D as a function of the magnitudes M and for different site-to-source distances R, indicated with different colors.

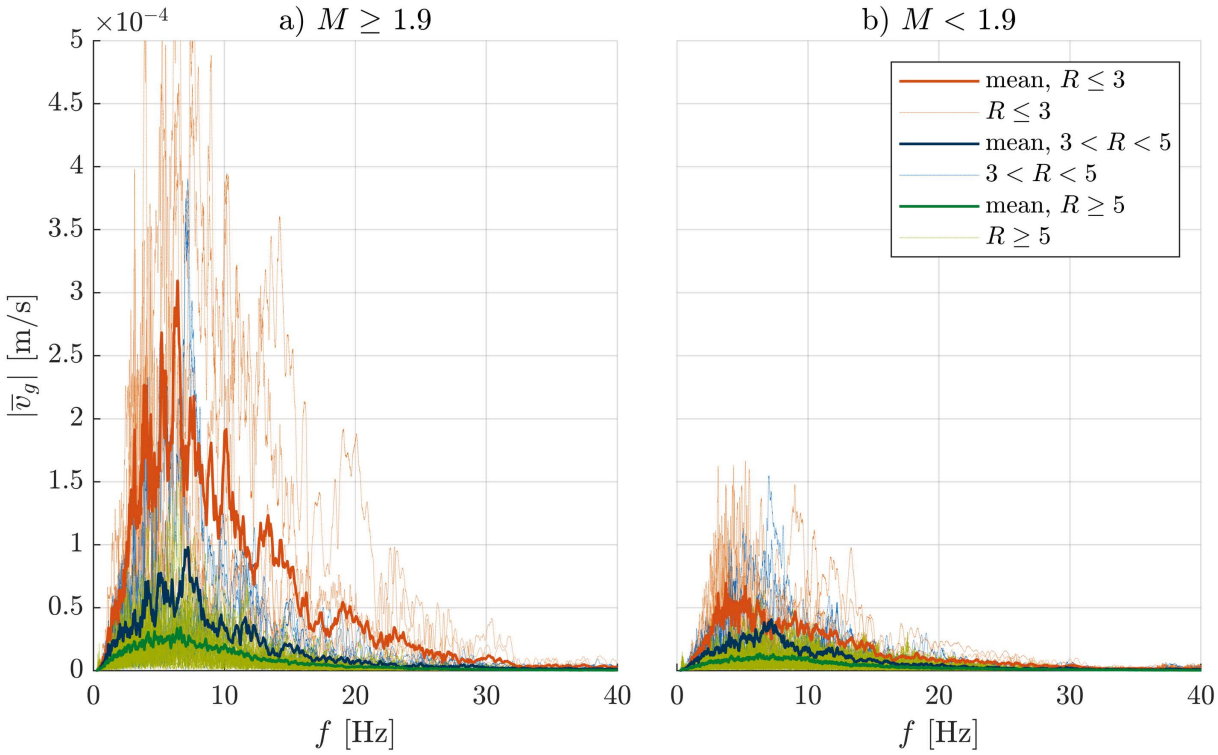

Figure 8: Absolute value of the spectra $|\overline{v}_g|$ of the **horizontal** velocity resultant as a function of the site-to-source distance R and magnitude M: a) $M \geq 1.9$, b) $M < 1.9$. The thin lines represent each single resultant, while the thick lines represent the mean for each distance category ($R \leq$3 km, 3 km$< R <$5 km,$R \geq$5 km).

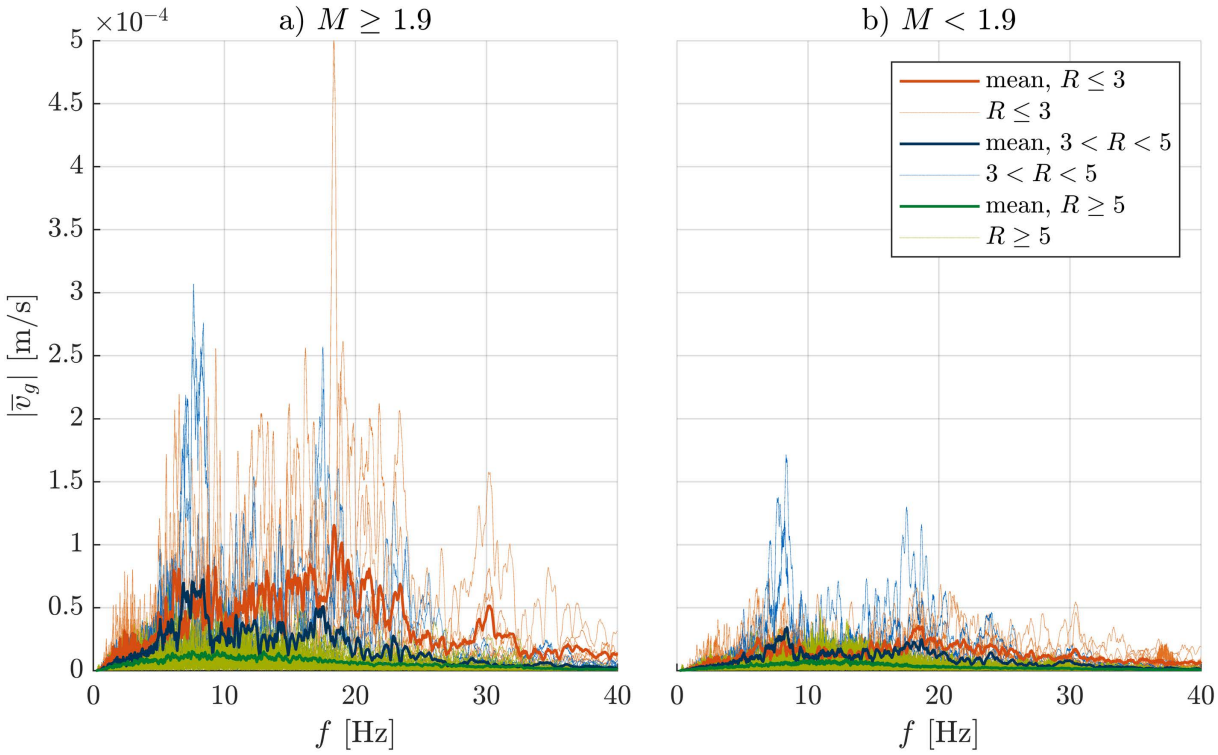

Figure 9: Absolute value of the spectra $|\overline{v}_g|$ of the **vertical** velocity as a function of the site-to-source distance R and magnitude M: a) $M \geq 1.9$, b) $M < 1.9$. The thin lines represent each single resultant, while the thick lines represent the mean for each distance category ($R \leq$3 km, 3 km$< R <$5 km,$R \geq$5 km).

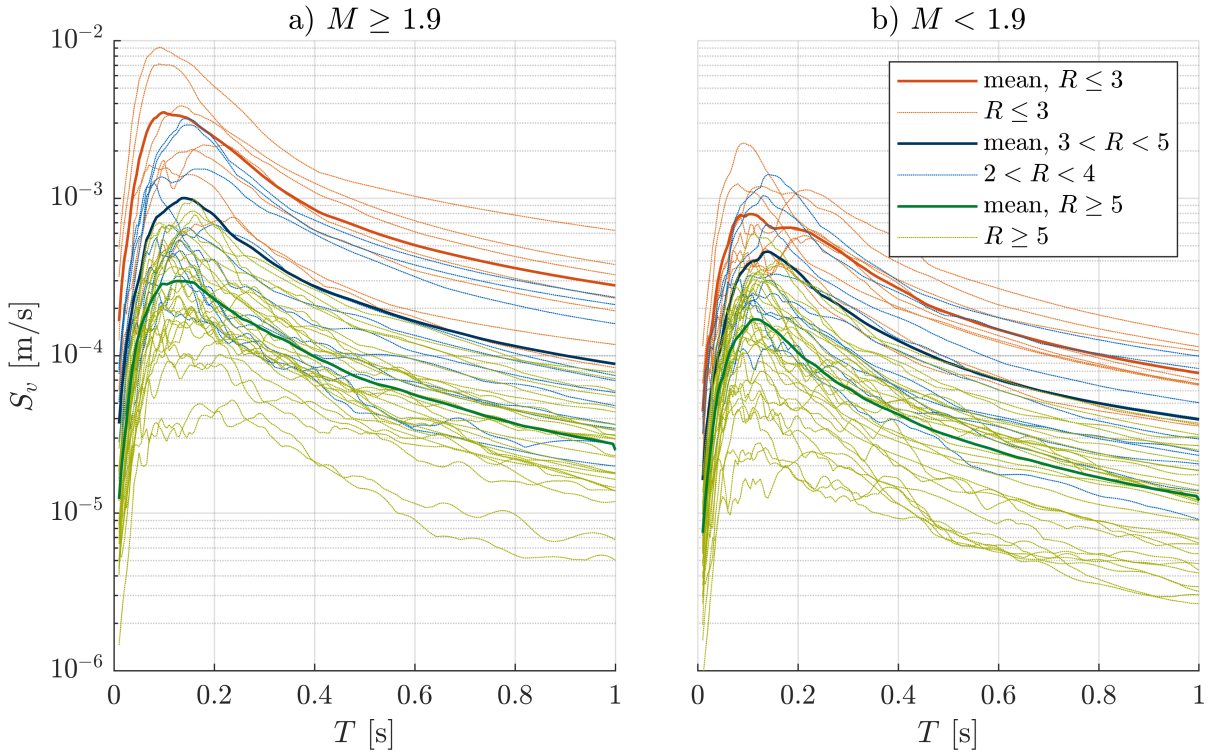

Figure 10: Elastic response spectra for the **horizontal** ground motions resultants as a function of the site-to-source distance R and magnitude M: a) $M \geq 1.9$, b) $M < 1.9$. The thin lines represent each single resultant, while the thick lines represent the mean for each distance category ($R \leq$3 km, 3 km$< R <$5 km,$R \geq$5 km).

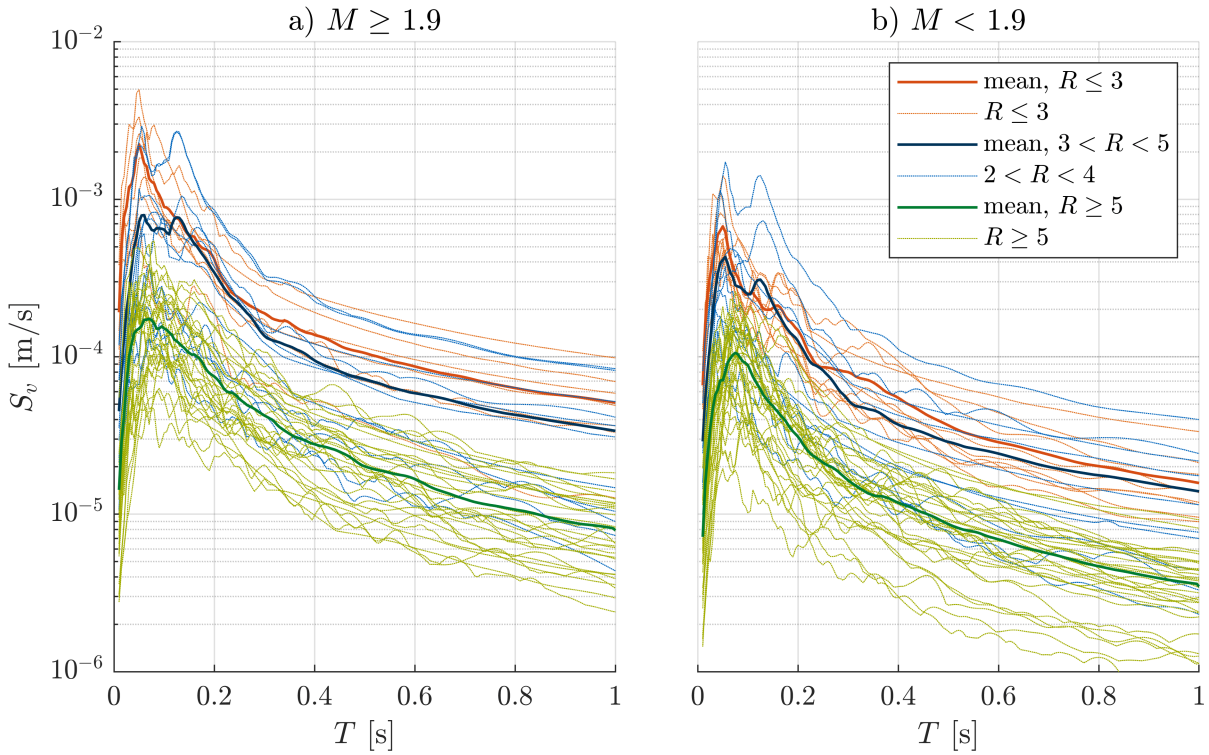

Figure 11: Elastic response spectra for the **vertical** ground motions resultants as a function of the site-to-source distance R and magnitude M: a) $M \geq 1.9$, b) $M < 1.9$. The thin lines represent each single resultant, while the thick lines represent the mean for each distance category ($R \leq$3 km, 3 km$< R <$5 km,$R \geq$5 km).

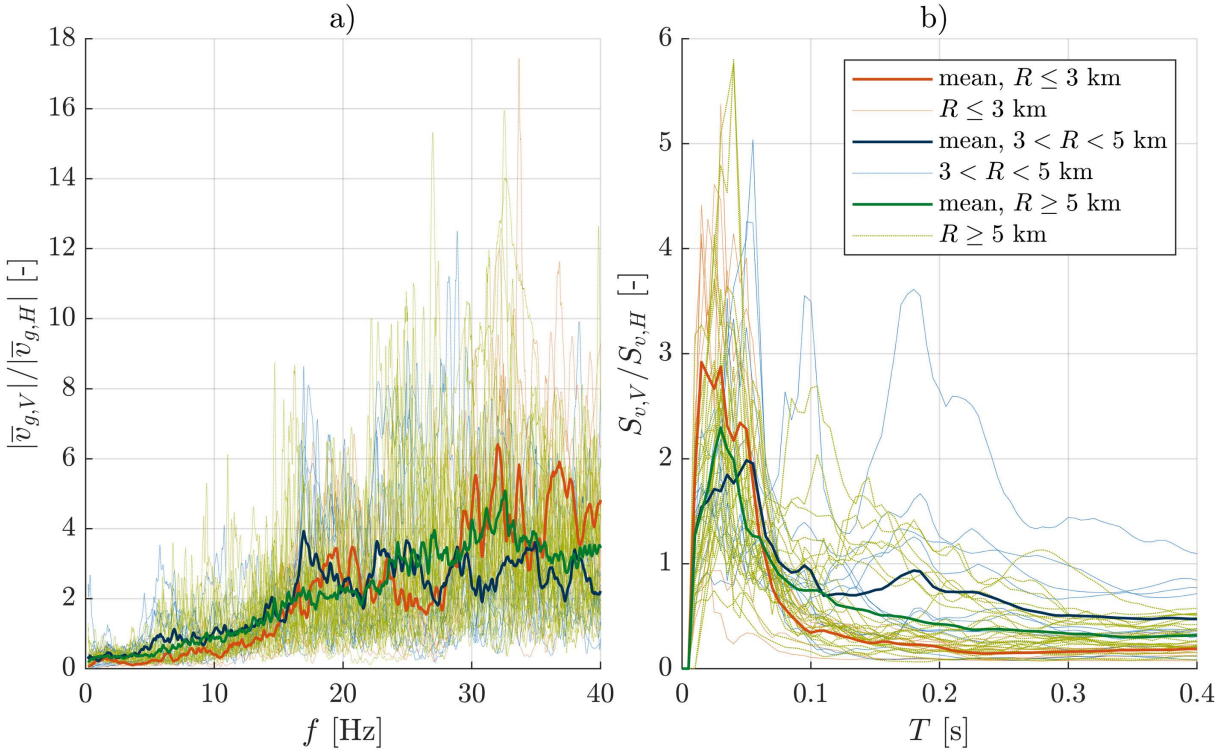

Figure 12: Vertical-to-horizontal (V/H) ratios as a function of the site-to-source distance R and $M \geq 1.9$: a) computed from the ground velocities, b) computed from the response spectra. The thin lines represent each single ratio, while the thick lines represent the mean for each distance category ($R \leq$3 km, 3 km$<$ $R <$5 km,$R \geq$5 km).

4.3 Elastic response spectra

Fig. 10 and Fig. 11 show the elastic response spectra for the ground motions as a function of the site-to-source distance R and magnitude M, for the horizontal and vertical direction respectively. For the horizontal direction, there is a clear separation between the spectra of the different R-categories and the curves are very smooth with maximum value around T=0.15 s. For the vertical direction, the curves for $R \leq$3 km and 3 km$<$ $R <$5 km cross each other and overlap at different T-intervals. This indicates that, the increase of vertical amplitudes with vicinity to the epicenter is not always confirmed. In some cases, the amplitude of the spectra for 3 km$<$ $R <$5 km exceed those for $R \leq$3 km. In vertical direction, the curves are less smooth, showing also amplification effects at different periods between 0.05 s and 0.15 s.

4.4 Vertical-to-horizontal ratio of the ground motions

To further investigate the relationship between horizontal and vertical inputs and responses, the vertical-to-horizontal ratio of the ground motions and the response spectra (only for $M \geq 1.9$) is analyzed.

Fig. 12a shows the V/H ratio computed from the ground velocities. This is lower than 1 for frequencies below 10 Hz, but, at frequencies higher than 15 Hz, can approach values as high as 6, especially for near-source recordings ($R \leq$3 km). Fig. 12b shows the V/H ratio computed from the elastic response spectra. At periods longer than 0.3 s, the ratio is approximately constant and generally less than 1. The maxima occur at periods between 0.01 and 0.1 s, following the trend of the V/H ratios for ground velocities, and can reach values of 3 for small R values. The smaller is R, the steeper is the decrease of the curves around the period $T \approx$0.6 s.

5 Conclusions

This contribution is concerned with the characterisation of the ground velocities for low-amplitude seismicity induced by geothermal operations, focusing on the seismological characteristics, the statistical evaluation of the spectral content and the elastic response spectra, for the case study of the Insheim geothermal reservoir in Germany,

It is shown, that the frequency ranges with maximum spectral amplitudes are different for the horizontal and vertical directions: the maxima of the horizontal spectra are concentrated in a narrow frequency range below 15 Hz, while the vertical spectra are spread over a broad frequency band up to 30 Hz. The latter aspect is particularly relevant because the fundamental modes of the vertical vibrations of the ceilings fall into the range of maximum vertical ground velocities.

It was found, that the V/H ratio strongly depends on the natural period and it is larger for periods below 0.1 s, following the trend of the ratio between the vertical and horizontal ground velocity spectra.

It can be concluded, that the vertical and horizontal components of the ground velocities are characterised by different frequency contents and could be treated separately: at frequencies above 15 Hz, the vertical component dominates the response, while at frequencies below 10 Hz it is clearly smaller than the horizontal one.

Future developments of these study will focus on extending the database for the Insheim geothermal reservoir and add new data from the Molasse basin in Bavaria, Germany.

Acknowledgements

The authors acknowledge the infrastructure and support of the Geothermal-Alliance Bavaria (GAB).

References

[1] J. R. R. Ritter and J. Groos, "Abschlussbericht mags-ep1, quantifizierung und charakterisierung des induzierten seismischen volumens im bereich landau/südpfalz," Joint project MAGS, Tech. Rep., 2014, available at https://www.mags-projekt.de/MAGS/DE/Downloads/MAGS_Abschlussbericht_EP1.pdf.

[2] BGR, "Federal institute for geosciences and natural resources," https://www.bgr.bund.de/EN/Themen/Erdbeben-Gefaehrdungsanalysen/Ingenieurseismologische_Gefaehrdungsanalysen/Induzierte_Seismizitaet/induzierte_seismizitaet_node_en.html.

[3] A. Khansefid, S. M. Yadollahi, G. Müller, F. Taddei, and A. Kumawat, "Seismic performance assessment of a masonry building under earthquakes induced by geothermal power plants operation," *Journal of Building Engineering*, vol. 48, p. 103909, 2022.

[4] G. Grünthal, "Induced seismicity related to geothermal projects versus natural tectonic earthquakes and other types of induced seismic events in central europe," *Geothermics*, vol. 52, pp. 22–35, 2014.

[5] G. Panza, F. Romanelli *et al.*, "Seismic ground motion modelling and damage earthquake scenarios: A bridge between seismologists and seismic engineers," 2002.

[6] S. Keil, A. Wilczek, and J. M. Wassermann, "Seismic microzonation of munich, germany, and implications for site amplification in case of induced seismicity," in *AGU Fall Meeting 2021*. AGU, 2021.

[7] A. Khansefid, S. M. Yadollahi, G. Müller, and F. Taddei, "Ground motion models for the induced earthquakes by the geothermal power plants activity," *Journal of Earthquake Engineering*, pp. 1–30, 2022.

[8] M. Vasterling, U. Wegler, J. Becker, A. Brüstle, and M. Bischoff, "Real-time envelope cross-correlation detector: application to induced seismicity in the insheim and landau deep geothermal reservoirs," *Journal of Seismology*, vol. 21, no. 1, pp. 193–208, 2017.

[9] L. Küperkoch, K. Olbert, and T. Meier, "Long-term monitoring of induced seismicity at the insheim geothermal site, germany," *Bulletin of the Seismological Society of America*, vol. 108, no. 6, pp. 3668–3683, 2018.

[10] M. Grund, J. C. Groos, and J. R. Ritter, "Fault reactivation analysis using microearthquake clustering based on signal-to-noise weighted waveform similarity," *Pure and applied geophysics*, vol. 173, no. 7, pp. 2325–2355, 2016.

[11] DIN, "Din 4150-2: Structural vibrations–part 3: Effects on structures," 1999.

[12] F. I. for Geosciences and N. Resources, "German regional seismic network (grsn)," https://www.seismologie.bgr.de/doi/grsn/.

[13] BGR, "Federal institute for geosciences and natural resources, channel inventory," https://eida.bgr.de/fdsnws/station/1/query?format=text&level=channel.

[14] G. Lanzano, L. Luzi, C. Cauzzi, J. Bienkowski, D. Bindi, J. Clinton, M. Cocco, M. D'Amico, J. Douglas, L. Faenza *et al.*, "Accessing european strong-motion data: An update on orfeus coordinated services," *Seismological Society of America*, vol. 92, no. 3, pp. 1642–1658, 2021.

[15] A. Strollo, D. Cambaz, J. Clinton, P. Danecek, C. P. Evangelidis, A. Marmureanu, L. Ottemöller, H. Pedersen, R. Sleeman, K. Stammler *et al.*, "Eida: The european integrated data archive and service infrastructure within orfeus," *Seismological Research Letters*, vol. 92, no. 3, pp. 1788–1795, 2021.

[16] A. Khansefid, A. Bakhshi, and A. Ansari, "Development of declustered processed earthquake accelerogram database for the iranian plateau: including near-field record categorization," *Journal of Seismology*, vol. 23, no. 4, pp. 869–888, 2019.

[17] S. Halbert, "Iris seed channel naming," https://ds.iris.edu/ds/nodes/dmc/data/formats/seed-channel-naming/.

[18] J. Groos, R. Fritschen, and J. Ritter, "Untersuchung induzierter erdbeben hinsichtlich ihrer spürbarkeit und eventueller schadenswirkung anhand der din 4150," *Bauingenieur*, vol. 88, pp. 374–384, 2013.

Appendix

A List of selected events and stations for the Insheim area

Table 3: List of selected events for the Insheim area.

Nr.	Origin Time	Mag.	Lat.	Long.	Depth [km]
-	2009-05-08T19:23:18	2.1	49.150	8.160	3
-	2009-05-08T20:33:09	2.0	49.150	8.150	3
-	2009-05-08T22:28:32	2.0	49.160	8.150	3
1	2009-10-18T19:12:12	1.5	49.148	8.164	5
2	2010-04-07T09:04:04	1.6	49.140	8.160	5
3	2010-04-07T13:46:21	1.7	49.140	8.160	5
-	2010-04-09T10:52:22	2.4	49.150	8.151	5
4	2010-04-09T12:36:33	2.2	49.148	8.157	5
5	2012-11-12T11:15:04	1.8	49.143	8.160	5
6	2012-11-12T12:53:02	1.5	49.141	8.157	5
7	2013-01-26T19:48:27	1.8	49.159	8.153	5
8	2013-02-17T20:07:15	2.0	49.161	8.152	4
9	2013-10-02T01:13:26	2.1	49.162	8.152	4
10	2013-11-18T12:54:15	1.5	49.144	8.146	6
11	2013-11-21T14:15:22	1.9	49.150	8.154	5
12	2016-02-12T06:26:04	1.7	49.146	8.150	5
13	2016-07-14T17:49:10	1.9	49.150	8.156	5

Table 4: Matrix of the stations which recorded the events, where each cross represents a set of 3 recordings in the 3 directions (Z, N, E). The cross between brackets indicates a discarded set of recordings.

StationEvent	1	2	3	4	5	6	7	8	9	10	11	12	13
INS1							x	x	x	x	x	x	
INS2					x	x	x	x	x	x	x		
INS3					x	x	x	x	x	x	x	x	x
INS4					x	x	x	x	x	x	x		
INS4B												x	x
INS5					x	x	x	x	x	x	x	x	x
INS6					x	x	x	x	x	x	x		
INS6B												x	x
INS7							x	x	x	x	x	x	x
INS8												x	x
INS9													
INSH					x	x	x	x	x	x	x	x	x
LDAU	x	x	x	(x)									
TMO20									x	x	x	x	x
TMO22									x	x	x		x
TMO54									x	x	x	x	x
TMO55									x	x	x	x	x
TMO57												x	x
TMO66												x	x
A127A													x